

Role of Surface Defects in Activation of O₂ and N₂O on ZrO₂ and Yttrium-Stabilized ZrO₂

Jianjun Zhu, Sander Albertsma, Jan G. van Ommen, and Leon Lefferts*

*Catalytic Processes and Materials, Faculty of Science and Technology, Institute of Mechanics, Processes And Control Twente (IMPACT), University of Twente, P.O. Box 217, 7500 AE Enschede, The Netherlands**Received: January 14, 2005; In Final Form: March 14, 2005*

The relationship between the structure of both yttrium-stabilized zirconia (YSZ) and ZrO₂ catalysts and their ability to activate N₂O and O₂ is studied by determination of catalytic properties and characterization with TPD, SEM, and XRD. Furthermore, the role of oxygen species formed via dissociation of either O₂ or N₂O in catalytic partial oxidation of methane (CPOM) is determined. N₂O can be activated at both structural defects (e.g., Zr cations located at corners) and intrinsic oxygen vacancies (Zr'_{Zr}-V_O^{••}-Zr'_{Zr}) and forms two types of oxygen species (α -O and β -O) on the surface, respectively. In contrast, molecular oxygen gives rise to only one type of oxygen species (β -O), that is, surface lattice oxygen. This type of oxygen species can be extracted by reaction with methane, forming the intrinsic oxygen vacancies again during CPOM. However, the structural defects are not active for oxygen activation during CPOM. Doping ZrO₂ with Y₂O₃ significantly decreases the number of structural defects via replacement of Zr⁴⁺ cations by Y³⁺ cations, located at corners, steps, kinks, and edges of the crystallites. Calcination at higher temperatures results in less structural defects due to both increasing crystallite size as well as transformation to more regular shaped crystallites. High temperature calcinations also increase the activity of YSZ in CPOM. This is attributed to the increase in the exposition of low index planes, especially those (111) with the lowest surface energy and the highest coordination numbers, induced by the thermal treatment.

Introduction

Natural gas is forecasted to outlast oil by about 60 years¹ despite the relatively underdeveloped state of the gas industry. Plenty of natural gas found in many locations around the world stimulates study on its utilization. Catalytic partial oxidation of methane (CPOM) to synthesis gas is an attractive process for conversion of natural gas to synthesis gas, as an alternative to steam reforming of methane. Most of the studies on CPOM were focused on metallic catalysts, such as supported cobalt, nickel, as well as noble metals (Rh, Pt). In contrast, irreducible metal oxides were hardly studied for CPOM, despite the fact that formation of synthesis gas is often observed as side reactions on oxide catalysts, for example, in the oxidative conversion of methane to methanol,^{2–4} formaldehyde,^{5,6} and methyl formate⁷ as well as oxidative coupling of methane.^{8,9}

The performance of hardly reducible oxides in CPOM, for example, ZrO₂ and yttrium-stabilized zirconia (YSZ), was reported in our previous work.^{10–13} Compared with metal catalysts, ZrO₂-based oxide catalysts are less active and selective. However, YSZ is a very stable catalyst, because of both thermal stability as well as prevention of evaporation of the catalyst, which takes place on metal catalysts. The low activity of YSZ can be compensated by introducing a second metal-based reforming catalyst.¹⁰ The metal catalyst is in this case protected from metal loss via evaporation of precious metal oxides because contact with oxygen at high temperatures is completely avoided.

A Mars-van Krevelen mechanism was proposed for CPOM over ZrO₂ and YSZ catalysts in our previous work,¹³ in which methane is oxidized by lattice oxygen ions (O_O^x) in the surface

layer. Extraction of the lattice oxygen ion results in formation of intrinsic oxygen vacancies (Zr'_{Zr}-V_O^{••}-Zr'_{Zr}) associated with two Zr³⁺ cations in the surface, which are replenished by molecular oxygen. YSZ contains a much higher concentration of extrinsic oxygen vacancies (Y'_{Zr}-V_O^{••}-Y'_{Zr}), both on the surface and in the bulk. This results, on one hand, in faster activation of oxygen on extrinsic vacancies at the surface and, on the other hand, in enhanced diffusion of oxygen ions through the bulk. This pathway appears faster than direct O₂ activation on intrinsic vacancies for ZrO₂, speeding up both oxygen activation as well as the reaction in CPOM.

Although previous work elucidated the role of both intrinsic and extrinsic defects in CPOM, the effect of the morphology of YSZ remains unclear. This work focuses on the role, if any, of structural defects (such as corners, edges, steps, and kinks) on ZrO₂ and YSZ. Therefore, in this study, the morphology of YSZ is modified and carefully characterized to reveal the effect on the interaction with oxygen as well as catalytic properties in CPOM. Second, N₂O is used as a probe molecule to study the nature of defects, as has been done on many defective oxides, for example, Li/MgO,¹⁴ Fe-ZSM5 zeolite,¹⁵ and ZrO₂.^{16,17} In short, the present work aims for identification of the structural requirements for CPOM over YSZ catalysts.

Experimental Section

Catalysts. All catalysts (YSZ14A, YSZ14B, YSZ14C, and ZrO₂) were prepared by calcining yttrium-stabilized zirconia (YSZ) or zirconia powder in air for 15 h, as described in our previous work.¹² In the sample code, YSZ means yttrium-stabilized zirconia, the number “14” refers to the weight percentage of Y₂O₃ in the sample, and A, B, and C denote the different calcination temperatures, 900, 1000, and 1100 °C,

* To whom correspondence should be addressed. E-mail: L.Lefferts@utwente.nl. Fax: +31-53-4894683.

TABLE 1: Results of N₂ Physical Adsorption, TPD of Oxygen, Estimation of the Surface Concentration of Zr (Estimated on the Basis of Stoichiometry and LEIS Measurements¹²), and Estimated Crystallite Sizes According to SEM and XRD (Line-Broadening) Measurements

catalysts	calcination temperature (°C)	S _g (m ² /g)	TPD of O ₂ species (atoms/m ²)		surface Zr* (atoms/m ²)	crystallite size (nm)	
			α-O	β-O		SEM	XRD
ZrO ₂	900	15.4	7.7 × 10 ¹⁶	4.7 × 10 ¹⁶	3.8 × 10 ¹⁸	~50	
YSZ14A	900	13.7	3.4 × 10 ¹⁶	3.4 × 10 ¹⁶		~50	39.4
YSZ14B	1000	10.2	1.8 × 10 ¹⁶	4.0 × 10 ¹⁶	2.9 × 10 ¹⁸	~75	61.1
YSZ14C	1100	7.0	1.2 × 10 ¹⁶	6.4 × 10 ¹⁶		~100	77.6

respectively. As described in our previous work,¹² TiO₂ and HfO₂ are two major contaminations in the bulk, whereas no inorganic contamination was detected on the outermost layer by low energy ion scattering (LEIS).

Catalytic Measurement. The catalytic performance of the catalysts was examined in a fixed-bed reactor made of an alumina tube (inner diameter, 4 mm; length, 450 mm) at atmospheric pressure. A mixture of 0.3 g of catalyst diluted with 0.3 g of α-Al₂O₃ particles was positioned in the isothermal zone of the reactor by quartz wool. The reactants, CH₄ and O₂, were diluted with helium (CH₄/O₂/He = 2:1:14), and the total flow rate was 170 mL/min (STP); GHSV was about 6 × 10³ h⁻¹. More details can be found in our previous work.¹¹

N₂O decomposition was carried out in the same setup as that used for CPOM. Diluted N₂O (N₂O/He = 3:14) was passed through the catalyst bed with a total flow rate of 170 mL/min (STP); GHSV was about 6 × 10³ h⁻¹. On-line gas chromatography with Carboxan 1000 and Haysep N columns was used to analyze the effluent gas from the reactor. Conversions (X) and yields (Y) were calculated according to the following.

For CPOM:

$$X_{\text{CH}_4} = \frac{\text{CH}_4^{\text{in}} - \text{CH}_4^{\text{out}}}{\text{CH}_4^{\text{in}}}; \quad X_{\text{O}_2} = \frac{\text{O}_2^{\text{in}} - \text{O}_2^{\text{out}}}{\text{O}_2^{\text{in}}}; \quad Y_{\text{CO}} = \frac{\text{CO}^{\text{out}}}{\text{CH}_4^{\text{in}}};$$

$$Y_{\text{CO}_2} = \frac{\text{CO}_2^{\text{out}}}{\text{CH}_4^{\text{in}}}; \quad Y_{\text{H}_2} = \frac{\text{H}_2^{\text{out}}}{2\text{CH}_4^{\text{in}}}; \quad Y_{\text{H}_2\text{O}} = \frac{\text{H}_2\text{O}^{\text{out}}}{2\text{CH}_4^{\text{in}}}$$

For N₂O decomposition:

$$X_{\text{N}_2\text{O}} = \frac{\text{N}_2\text{O}^{\text{in}} - \text{N}_2\text{O}^{\text{out}}}{\text{N}_2\text{O}^{\text{in}}}$$

TPD of Adsorbed Oxygen Species. Temperature-programmed desorption (TPD) experiments were carried out using a homemade vacuum-TPD setup equipped with a mass spectrometer (BALZERS QMS 200F). The adsorbed oxygen species were formed either via dissociative adsorption of N₂O on the catalyst or via oxidation of the catalyst with O₂. The O₂ MS signal was normalized by the surface area of the catalyst sample. For quantitative estimation of desorbed oxygen, the on-line mass spectrometer was calibrated for O₂.

In the case of N₂O dissociative adsorption, the experiment was conducted according to the following procedure: About 0.15 g of catalyst was placed in a quartz tube (reactor). The catalyst was preactivated at 800 °C and at 10⁻³ mbar for 3 h and subsequently cooled to 300 °C. After the preactivation, N₂O was introduced (7 mbar). The reactor was held at 300 °C for 2 h. Subsequently, the system was cooled to 50 °C and evacuated at 50 °C for 2 h to remove weakly adsorbed species. Then, TPD was carried out with a heating rate of 10 °C/min to 800 °C and dwelled at 800 °C for 10 min. Adsorption at 300 °C for 2 h is sufficient to reach equilibrium, because longer adsorption times resulted in identical amounts of adsorbed oxygen.

In the case of oxidation with O₂, the sample was preactivated at 800 °C and 10⁻³ mbar for 3 h first, followed by treatment with pure O₂ at 7 mbar and 800 °C for 2 h. Subsequently, the system was slowly cooled to 50 °C under 7 mbar of O₂ and evacuated for 2 h. Finally, TPD was carried out with the same conditions as those mentioned above.

BET Surface Area. The specific surface area (SBET) of the samples was determined from the adsorption and desorption isotherms of N₂ at -196 °C using an ASAP 2400 (Micromeritics) instrument. The BET surface areas for all catalysts used in the present work are listed in Table 1.

SEM and XRD. The structure of the samples was determined with powder X-ray diffraction (XRD, Philips PW1830). The diffraction patterns were obtained with nickel-filtered Cu Kα1 radiation (λ = 1.5405 Å) at a scanning speed of 2° in 2θ min⁻¹. The morphology of the catalyst particle was studied with scanning electron microscopy (SEM) (LEO 1550 FEG SEM).

Results

CPOM. CPOM was carried out over ZrO₂ and three YSZ catalysts calcined at different temperatures. Methane conversions as a function of reaction temperature over four catalysts are compared in Figure 1. Almost complete oxygen conversion is achieved at about 700 °C for all catalysts (not shown here). Before oxygen is consumed completely at temperatures below 700 °C, CH₄ conversion increases with reaction temperature rapidly, whereas a slight increase in CH₄ conversion is observed after oxygen is depleted at 700 °C and above. Compared with ZrO₂, all three YSZ catalysts show much higher activities for CPOM. The three YSZ catalysts show only small differences in CH₄ conversion rate when based on catalyst weight. However, the activity per square meter of these three YSZ catalysts varies significantly. The CH₄ conversion rates at 600 °C were estimated to be 8.4 × 10¹⁷, 9.2 × 10¹⁷, and 12.6 × 10¹⁷ mol·m⁻²·s⁻¹ for YSZ14A, YSZ14B, and YSZ14C, respectively. According to the usual criteria (the Carberry number and the Wheeler–Weisz

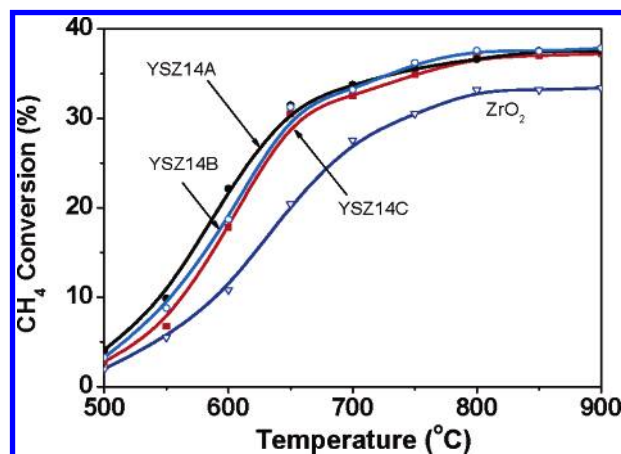


Figure 1. CH₄ conversion as a function of reaction temperature. Catalysts: ZrO₂, YSZ14A, YSZ14B, and YSZ14C. Feed: CH₄/O₂/He = 2:1:14; total flow rate, 170 mL/min.

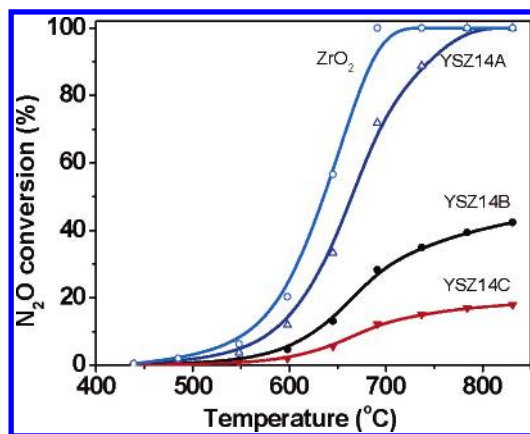


Figure 2. N₂O conversion as a function of reaction temperature. Catalysts: ZrO₂, YSZ14A, YSZ14B, and YSZ14C. Feed: N₂O/He = 3:14; total flow rate, 170 mL/min.

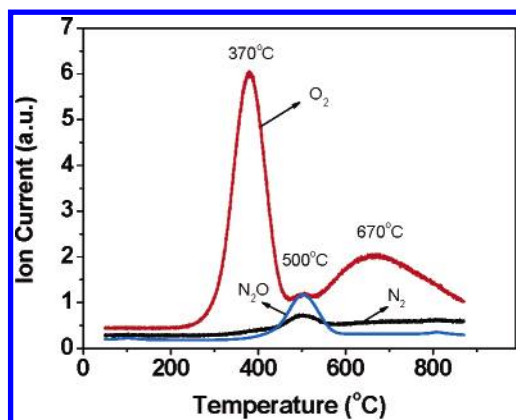


Figure 3. TPD profiles obtained after N₂O decomposition over ZrO₂ (S_g = 15.4 m²/g) at 300 °C for 2 h. The intensity is normalized by surface area.

modulus¹⁸), it can be concluded that mass transfer limitation can be neglected at 600 °C. Apparently, high temperature calcination increases the rate per square meter.

Decomposition of N₂O. Steady state decomposition of N₂O was carried out over ZrO₂ and three YSZ catalysts at temperatures from 400 to 850 °C. N₂O conversions are shown as a function of temperature in Figure 2. All four catalysts start to decompose N₂O at about 450 °C. Compared with YSZ catalysts, ZrO₂ is much more active for N₂O decomposition. Complete conversion of N₂O is observed over ZrO₂ at about 700 °C, while only about 70, 28, and 12% of the N₂O is converted over YSZ14A, YSZ14B, and YSZ14C, respectively. The activity appears to decrease with increasing calcination temperature for YSZ catalysts. A blank experiment showed that N₂O conversion over α -Al₂O₃ was less than 1% at 750 °C, indicating that contributions of both gas phase reaction and α -Al₂O₃ can be neglected.

TPD of Adsorbed Oxygen Species. Figure 3 shows the TPD profiles of adsorbed oxygen species formed via decomposition of N₂O over ZrO₂ at 300 °C. The TPD result reveals that two types of oxygen species are present on ZrO₂: α -O (desorption peak at 370 °C) and β -O (desorption peak at 670 °C). Note that α -O mentioned in the present work is not related to α -oxygen as defined for Fe/ZSM515, although both species are formed out of N₂O. A small N₂O desorption peak is observed at 500 °C, accompanied by small N₂ and O₂ peaks.

TPD profiles of oxygen formed via N₂O decomposition and via oxidation with O₂ are compared in Figure 4. A blank experiment was also carried out over ZrO₂ after activation at

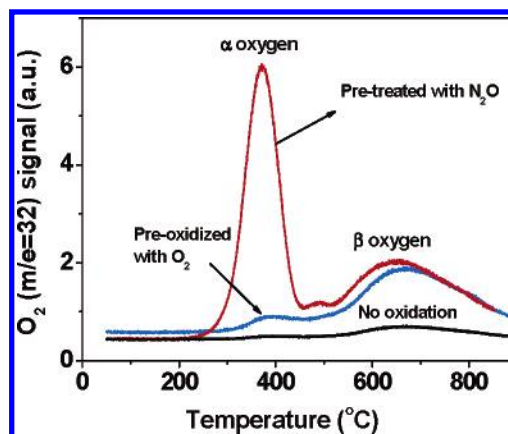


Figure 4. TPD profiles of oxygen species formed via N₂O decomposition and via preoxidation with O₂. The intensity is normalized by surface area.

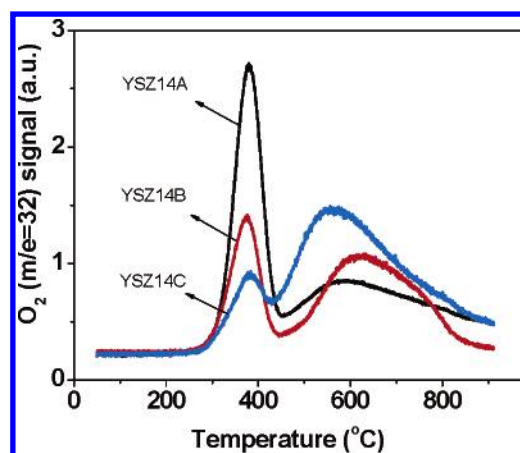


Figure 5. TPD profiles of oxygen species formed via decomposition of N₂O over YSZ14A, YSZ14B, and YSZ14C. The intensity is normalized by surface area.

800 °C and cooling to 50 °C at 10⁻³ mbar during 3 h. Almost no desorption of oxygen species is observed during the blank experiment. In contrast, when ZrO₂ is treated by either N₂O at 300 °C or by O₂ at temperature between 50 and 800 °C, two oxygen desorption peaks are obtained at identical desorption temperatures (370 and 670 °C). However, treatment with N₂O results in much more α -O on ZrO₂ as compared to treatment with O₂, whereas almost identical amounts of the β -O are formed out of N₂O and O₂.

TPD profiles of oxygen species formed via decomposition of N₂O are compared in Figure 5 for three YSZ catalysts calcined at different temperatures. The intensity of MS signals was normalized by the surface area of the catalyst. Compared with ZrO₂ in Figure 4, much less α -O desorbs from all YSZ14 catalysts. Moreover, the amount of α -O decreases with increasing calcination temperature (YSZ14A > YSZ14B > YSZ14C), but the amount of β -O increases concurrently. Furthermore, the desorption temperature of β -O seems to decrease with increasing calcination temperature. The amounts of both types of oxygen are estimated on the basis of the peak areas (Table 1).

Characterization. The morphology of catalyst particles is shown in Figure 6. The crystallite sizes of YSZ14A, YSZ14B, and YSZ14C, estimated on the basis of their SEM images, are in the order of nanometers and increase with increasing calcination temperature. The estimated particle sizes are 50 nm for YSZ14A, 75 nm for YSZ14B, and about 100 nm for YSZ14C. Moreover, calcination at higher temperature also

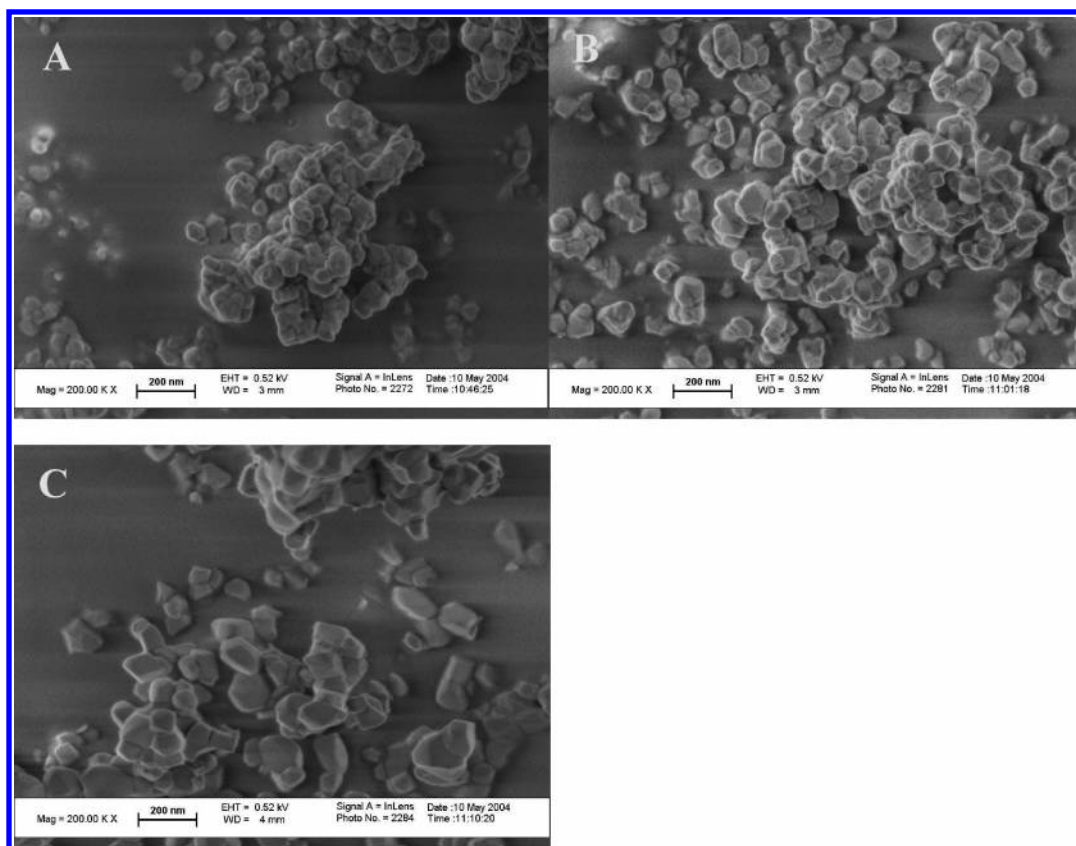


Figure 6. SEM micrographs of YSZ14A calcined at 900 °C (A), YSZ14B calcined at 1000 °C (B), and YSZ14C calcined at 1100 °C (C).

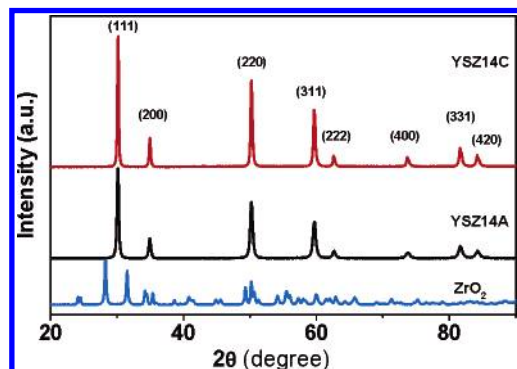


Figure 7. XRD patterns of ZrO₂ and YSZ catalysts.

results in more regular shaped crystallites with an apparent increasing presence of low index planes.

XRD patterns of ZrO₂, YSZ14A, and YSZ14C are shown in Figure 7. All YSZ catalysts possess the cubic crystallite structure, whereas the ZrO₂ structure is monoclinic. On the basis of the most intensive Bragg peak ($2\theta = 30.14^\circ$) of the XRD spectrum, the grain size was also estimated by the Scherer equation. As shown in Table 1, the particle sizes estimated on the basis of both XRD and SEM are in reasonable agreement.

Discussion

Surface Oxygen Species. TPD of oxygen formed via decomposition of N₂O revealed the presence of two types of oxygen species, desorbing from the surfaces of ZrO₂ and YSZ catalysts (α -O and β -O species). YSZ14A and ZrO₂ have almost identical surface areas and comparable particle sizes. However, the amount of α -O atoms desorbed from ZrO₂ is about double as compared with YSZ14A (Table 1). Apparently, the number of sites able to dissociatively adsorb N₂O decreases as a result

of doping ZrO₂ with Y₂O₃. This indicates that the α -O atoms are associated to Zr, rather than to Y. As shown in Figure 5 and Table 1, the amount of α -O per square meter decreases with decreasing specific surface area (YSZ14A > YSZ14B > YSZ14C). This difference must be caused by the change in structure of the surface of the catalysts because the surface composition is known to remain unchanged, as reported previously.¹² Therefore, we conclude that α -O atoms are adsorbed at structural defects with low oxygen coordination numbers, for example, corners, edges, kinks, and steps, as the amount of α -O decreases with increasing crystallite size and with increasing regularity of the crystallite shape (Table 1, Figure 6). Doping Y₂O₃ in ZrO₂ causes the amount of α -O to decrease much more than what one would expect from the fact that the surface coverage of Y₂O₃ is only 14% (mol %). Apparently, yttrium resides preferentially on the structural defects, effectively replacing Zr with Y at these sites, thus preventing the formation of α -O.

On the basis of the surface composition measured by LEIS,¹² the total number of Zr cations per square meter is estimated for both monoclinic ZrO₂ and cubic YSZ catalysts (Table 1). The amount of α -O is as low as 2% of the surface zirconium cations for ZrO₂ and even less for all YSZ samples (1.2, 0.6, and 0.4% for YSZ14A, YSZ14B, and YSZ14C, respectively). The fact that α -O is a minority species is in agreement with the conclusion above that α -O resides on low coordination sites as the order of magnitude agrees with what one would expect for edges, corners, kinks, and steps on the not too well defined crystals shown in Figure 6. Zhao et al.¹⁹ studied the nature of different Zr sites on ZrO₂ by ESR and reported that corners of ZrO₂ crystallites are mainly Zr³⁺ cations. Miller et al.²⁰ studied N₂O adsorption and decomposition on ZrO₂ with FT-IR and observed that the number of surface Zr³⁺ sites significantly decreased when the surface of ZrO₂ was exposed to N₂O at

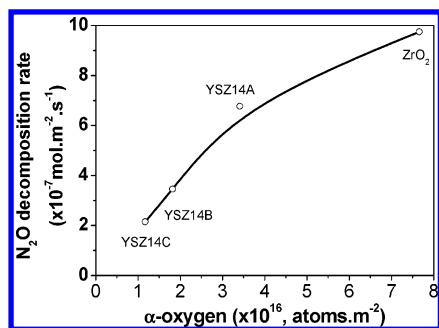


Figure 8. Dependence of N_2O conversion rate on the amount of $\alpha\text{-O}$ observed during TPD.

350 °C. This was attributed to oxygen atoms formed via the dissociation of N_2O ; however, no distinction was made between the intrinsic oxygen vacancies and the structural defects (e.g., corners).

Adsorption of molecular N_2O at Zr^{4+} sites on the surface of ZrO_2 was observed by Miller et al.¹⁷ with FT-IR spectroscopy, which is in agreement with the small amount of N_2O desorbed at about 500 °C from ZrO_2 (Figure 4). Simultaneous formation of O_2 and N_2 at 500 °C might be caused by decomposition of the desorbing N_2O at active sites, which are regenerated by desorption of $\alpha\text{-O}$ at temperatures above 370 °C.

The amounts of the $\beta\text{-O}$ formed during TPD correspond to 0.62 and 0.47% of oxygen ions in one monolayer of ZrO_2 and YSZ, respectively. It was reported previously¹³ that about 13.6 and 8.5% of oxygen ions in the outermost layer can be extracted from ZrO_2 and YSZ, respectively, by H_2 or CH_4 at 900 °C, conditions that cause a much lower effective oxygen pressure as compared to vacuum used in the present work. Therefore, this small amount of $\beta\text{-O}$ can be reasonably attributed to partial reduction of the surface at high temperatures under high vacuum, forming oxygen vacancies ($\text{Zr}'_{\text{Zr}}\text{-V}_{\text{O}}^{\bullet\bullet}\text{-Zr}'_{\text{Zr}}$). Consistently, Deibert et al.²¹ observed reduction of the ZrO_2 surface layer after exposure to UHV at temperatures above 550 °C. It is also important to note that there is also mounting evidence from others that the surface of ZrO_2 can be partly reduced by reducing gases, for example, CO ,^{22,23} although ZrO_2 is not normally considered to be reducible.

Activation of N_2O and O_2 . Figure 8 shows that the decomposition rate of N_2O over ZrO_2 and YSZ at 600 °C increases with the surface concentration of $\alpha\text{-O}$ as determined by TPD. This strongly suggests that the structural defects (corners, edges, kinks, and steps) are active sites for N_2O decomposition. The presence of Y_2O_3 in the surface decreases both the number of adsorption sites as discussed in section 4.1 and the number of active sites.

It is well-known that extrinsic oxygen vacancies ($\text{Y}'_{\text{Zr}}\text{-V}_{\text{O}}^{\bullet\bullet}\text{-Y}'_{\text{Zr}}$) are generated by doping ZrO_2 with Y_2O_3 as the effective charge of the incorporation of two Y^{3+} ions is balanced with an oxygen vacancy.^{24,25} However, the significant lower activity of YSZ (Figure 2), as compared with ZrO_2 , implies that these extrinsic oxygen vacancies are not active sites for N_2O decomposition.

Desorption of oxygen from ZrO_2 (Figure 3) and YSZ (Figure 5) clearly showed that decomposition of N_2O already occurred at temperatures as low as 300 °C. Comparable results have been reported even for room temperature.^{16,20} However, N_2O conversion at temperatures below 450 °C at GHSV of $6 \times 10^3 \text{ h}^{-1}$ is below the detecting limit in this work (Figure 2). Oxygen vacancies were generally proposed as the active sites for N_2O decomposition over many oxides, for example, ZrO_2 ,¹⁶ $\text{YBa}_2\text{Cu}_3\text{O}_7$, and Gd_2CuO_4 .²⁶ Miller et al.²⁰ proposed that decomposition of

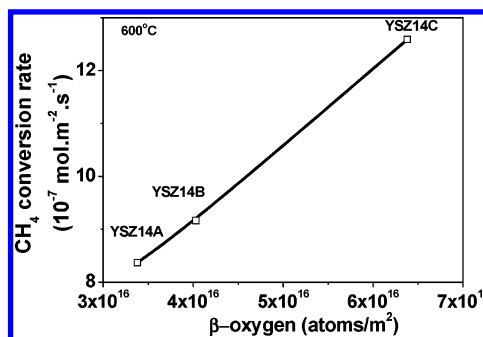


Figure 9. Dependence of methane conversion rate on the amount of $\beta\text{-O}$ observed during TPD.

N_2O over ZrO_2 proceeds via an electron transfer reaction from the Zr^{3+} site to form N_2O^- as a transient intermediate, which decomposes to molecular N_2 and an adsorbed oxygen atom.

The amount of $\beta\text{-O}$ on ZrO_2 is identical after oxidation with either N_2O or O_2 . This indicates that the surface oxygen vacancies ($\text{Zr}'_{\text{Zr}}\text{-V}_{\text{O}}^{\bullet\bullet}\text{-Zr}'_{\text{Zr}}$) formed by partial reduction (removal of surface lattice oxygen ions via high temperature vacuum treatment) are able to activate both N_2O and O_2 . This is consistent with our previous conclusion¹³ that molecular oxygen is directly activated on this type of oxygen vacancies, based on the observation that $\text{C}^{18}\text{O}^{16}\text{O}$ was produced during $^{18}\text{O}_2\text{-CH}_4$ pulse over ZrO_2 at 600 °C. However, almost no $\alpha\text{-O}$ desorbed from ZrO_2 oxidized with O_2 at temperatures between 50 and 800 °C (Figure 4). This indicates that oxygen molecules hardly dissociate at the structural defective sites (e.g., corners and edges) at temperatures below the desorption temperature of $\alpha\text{-O}$. Similar observations were also reported by Nakamura et al.²⁷ for CaO treated with either N_2O or O_2 . It was proposed by Winter²⁸ that one-electron defects are responsible for N_2O activation, while activation of O_2 occurs mainly at two-electron vacancies. Intrinsic oxygen vacancies ($\text{Zr}'_{\text{Zr}}\text{-V}_{\text{O}}^{\bullet\bullet}\text{-Zr}'_{\text{Zr}}$) are associated with two Zr^{3+} cations, as opposed to an isolated structural defective site at corners and edges, that can supply only one electron. This explains why structural defects are *not* active sites for oxygen activation during CPOM, although they can adsorb N_2O dissociatively. This conclusion is also supported by the fact shown in Figure 1 that ZrO_2 is less active in CPOM than YSZ catalysts, although ZrO_2 has more structural defective sites than YSZ, as discussed above.

Effect of Calcination Temperature. The methane conversion rate per square meter increases with increasing calcination temperature (Figure 1), although these catalysts have identical bulk compositions as well as surface compositions ($12 \pm 2 \text{ mol } \% \text{ Y}_2\text{O}_3$ in the outermost layer).¹² The amounts of $\beta\text{-O}$ desorbed from YSZ14 catalysts also increase with increasing calcination temperature (Figure 5, Table 1). Figure 9 demonstrates a linear relationship between the methane conversion rate per square meter and the amount of $\beta\text{-O}$.

This leaves the question of why the activity and amount of $\beta\text{-O}$ increase with calcination temperature. SEM images of three YSZ catalysts showed that calcination at higher temperature results in more regular shaped crystallites with an increasing presence of low index planes (Figure 6), suggesting that low index planes contain more $\beta\text{-O}$. The formation of low index planes during thermal treatment is well-known. It was reported that the oxygen-terminated (111) surface of oxides with the fluorite structure is energetically favorable, since this structure does not create a dipole moment.²⁹ Indeed, the (111) face has the lowest surface energy for cubic YSZ (with the fluorite structure)³⁰ as compared to the (110) and (100) faces. Therefore,

especially the exposure of (111) planes is expected to increase with calcination temperature. The same trend was also reported for monoclinic ZrO₂ by Morterra et al.³¹

Figure 5 demonstrated that more active catalysts appear to desorb not only more β -O but also more easily, that is, at lower temperatures. We propose that the surface reducibility of YSZ increases with the coordination number of zirconium cation in the surface. The coordination number of zirconium cation depends on the orientation of the surface plane. On the (111) surface face, Zr is coordinated with 7 oxygen ions, while the coordination numbers are 6 for Zr on both the (110) and (100) surface faces as compared to 8 in the bulk.³⁰ As discussed above, the most stable surface seems indeed to be the surface with the highest coordination number. It seems reasonable to assume that surface lattice oxygen is more easily removed when the original coordination number is high. The results in Figure 5 indicate that the average coordination number of Zr in the surface of YSZ increases with calcination temperature and that therefore surface lattice oxygen is easier to be extracted, enhancing the activity for CPOM.

Conclusion

The role of defective structure of both ZrO₂ and YSZ in activation of O₂ and N₂O has been studied. N₂O can be activated at both structural defects (e.g., Zr cations located at corners) and intrinsic oxygen vacancies (Zr'_{Zr}-V_O^{••}-Zr'_{Zr}) and forms two types of oxygen species (α -O and β -O) on the surface, respectively. In contrast, molecular oxygen gives rise to only one type of oxygen species (β -O), that is, surface lattice oxygen. This type of oxygen species can be extracted by reaction with methane, forming the intrinsic oxygen vacancies again during CPOM. However, the structural defects are not active for oxygen activation during CPOM. Doping ZrO₂ with Y₂O₃ significantly decreases the number of structural defects via replacement of Zr⁴⁺ cations by Y³⁺ cations, located at corners, steps, kinks, and edges of the crystallites. Calcination at higher temperatures results in less structural defects due to both increasing crystallite size as well as transformation to more regular shaped crystallites. High temperature calcination also increases the activity of YSZ in CPOM. This is attributed to the increase in the exposition of low index planes, especially those (111) with the lowest surface energy and the highest coordination numbers, induced by the thermal treatment.

Acknowledgment. This work was performed under the auspices of NIOK, The Netherlands Institute of Catalysis Research. Stichting Technische Wetenschappen (STW, the Dutch technology foundation) is gratefully acknowledged for

financial support under project number UPC-5037. The authors thank Dr. Henny J. M. Bouwmeester (IMS, University of Twente, The Netherlands) for valuable discussion, Ing. J. A. M. Vrielink, Dr. R. Keim, and Mr. H. Koster for BET, SEM, and XRD measurements, respectively, and Ing. Bert Geerdink for technical support.

References and Notes

- (1) Cornot-Gandolphe, S. *Energy Explor. Exploit.* **1995**, *13*, 3.
- (2) Chun, J. W.; Anthony, R. G. *Ind. Eng. Chem. Res.* **1993**, *32*, 259.
- (3) Sugino, T.; Kido, A.; Azuma, A.; Ueno, A.; Udagawa, Y. *J. Catal.* **2000**, *190*, 118.
- (4) Zhang, Q.; He, D.; Han, Z.; Zhang, X.; Zhu, Q. *Fuel* **2002**, *81*, 1599.
- (5) Weng, T.; Wolf, E. E. *Appl. Catal. A* **1993**, *96*, 383.
- (6) Parmaliana, A.; Arena, F. *J. Catal.* **1997**, *167*, 57.
- (7) Parmaliana, A.; Frusten, F.; Arna, F.; Mezzapica, A.; Sokolovskii, V. *Catal. Today* **1998**, *46*, 117.
- (8) Campbell, K. D.; Zhang, H.; Lundford, J. H. *J. Phys. Chem.* **1988**, *92*, 750.
- (9) Wada, S.; Tagawa, T.; Imai, H. *Appl. Catal.* **1989**, *47*, 277.
- (10) Zhu, J.; Rahuman, M. S. M. M.; van Ommen, J. G.; Lefferts, L. *Appl. Catal., A* **2004**, *259*, 95.
- (11) Zhu, J.; van Ommen, J. G.; Lefferts, L. *J. Catal.* **2004**, *225*, 388.
- (12) Zhu, J.; van Ommen, J. G.; Knoester, A.; Lefferts, L. *J. Catal.* **2005**, *230*, 291.
- (13) Zhu, J.; van Ommen, J. G.; Bouwmeester, H. J. M.; Lefferts, L. *Angew. Chem.*, submitted for publication, 2005. Zhu, J. Ph.D. Thesis, University of Twente, The Netherlands, 2005.
- (14) Nakamura, M.; Yanagibashi, H.; Mitsuhashi, H.; Takezawa, N. *Bull. Chem. Soc. Jpn.* **1993**, *66*, 2467.
- (15) Panov, G. I.; Sobolev, V. I.; Kharitonov, A. S. *J. Mol. Catal.* **1990**, *61*, 85.
- (16) Lin, J.; Chen, H. Y.; Chen, L.; Tan, K. L.; Zeng, H. C. *Appl. Surf. Sci.* **1996**, *103*, 307.
- (17) Miller, T. M.; Grassian, V. H. *J. Am. Chem. Soc.* **1995**, *117*, 110969.
- (18) van Santen, R. A.; van Leeuwen, P. W. N. M.; Moulijn, J. A.; Averill, B. A. *Catalysis: An integrated approach*; Elsevier: Amsterdam, The Netherlands, 1999.
- (19) Zhao, Q.; Wang, X.; Cai, T. *Appl. Surf. Sci.* **2004**, *225*, 7.
- (20) Miller, T. M.; Grassian, V. H. *Catal. Lett.* **1997**, *46*, 213.
- (21) Deibert, M. C.; Kahraman, R. *Appl. Surf. Sci.* **1989**, *37*, 327.
- (22) Stagg, S. M.; Romeo, E.; Padro, C.; Resasco, D. E. *J. Catal.* **1998**, *178*, 137.
- (23) Sharma, S.; Hilaire, S.; Vohs, J. M.; Gorte, R. J.; Jen, H. W. *J. Catal.* **2000**, *190*, 199.
- (24) Mommer, N.; Lee, T.; Gardber, J. A.; Evenson, W. E. *Phys. Rev. B* **2000**, *61*, 162.
- (25) Karaoetrova, E.; Platzer, R.; Gardner, J. A.; Schutfort, E.; Sommers, J. A.; Evenson, W. E. *J. Am. Ceram. Soc.* **2001**, *84*, 65.
- (26) Belapurkar, D.; Gupta, N. M.; Phatak, G. M.; Iyer, R. M. *J. Mol. Catal.* **1994**, *87*, 287.
- (27) Nakamura, M.; Mitsuhashi, H.; Takezawa, H. *J. Catal.* **1992**, *138*, 686.
- (28) Winter, E. R. S. *J. Catal.* **1974**, *34*, 431.
- (29) Conesa, J. C. *Surf. Sci.* **1995**, *339*, 337.
- (30) Ballabio, G.; Bernasconi, M.; Pietrucci, F.; Serra, S. *Phys. Rev. B* **2004**, *70*, 075417.
- (31) Cerrato, G.; Bordiga, S.; Barbera, S.; Morterra, C. *Surf. Sci.* **1997**, *377–379*, 50.